

PHYSICS-GUIDED DATA EXPANSION FOR PHOTOCATHODES USING TESS TRANSVERSE MOMENTUM MEASUREMENTS

S. Malhotra^{*,1,2}, L. B. Jones^{2,3}, N. Kumar^{1,2}, C. P. Welsch^{1,2}

¹Department of Physics, University of Liverpool, Liverpool, United Kingdom

²The Cockcroft Institute, Warrington, United Kingdom

³ASTeC, Daresbury Laboratory, STFC, Warrington, United Kingdom

Abstract

Precise characterisation of photocathode mean transverse energy is critical for optimising electron beam quality. This paper presents a physics-informed image processing pipeline using Transverse Energy Spread Spectrometer data (231–291 nm), incorporating Gaussian Point Spread Function fitting, Wiener deconvolution, resolution equalisation via reblurring, and physics informed noise-aware augmentation. A high-fidelity dataset of 6500 synthetic images was generated, achieving average SSIM = 0.997 and $R^2 \approx 0.98$, enabling robust MTE prediction and supporting future ML-based diagnostics for next-generation photoinjectors.

INTRODUCTION

In electron accelerators, beam emittance governs brightness. This is fundamentally limited by the electron transverse momenta at the photocathode, p_x and p_y as follows:

$$\varepsilon_{nx,\text{rms}} = \frac{\sigma_x \sqrt{\langle p_x^2 \rangle}}{mc} \quad \text{and} \quad \varepsilon_{ny,\text{rms}} = \frac{\sigma_y \sqrt{\langle p_y^2 \rangle}}{mc}. \quad (1)$$

Reducing $\langle p_{x,y}^2 \rangle$ is essential to achieve sub-0.5 $\mu\text{m}/\text{mm}$ emittance from photocathodes [1]. Both the mean transverse energy (MTE) and mean longitudinal energy (MLE) originate from the intrinsic emittance of the photocathode, which is mainly governed by the material's surface morphology and the excess energy imparted to each electron at the instant of photoemission. This is the difference between the incident photon energy and the material work function [2, 3].

The ability to measure the transverse component of the excess energy of emitted electrons facilitates research to characterise existing and new photocathode materials, and to reduce intrinsic emittance.

The Transverse Energy Spread Spectrometer (TESS) developed by the ASTeC at STFC Daresbury Laboratory is specifically designed to measure the MTE by acquiring the transverse energy distribution curve (TEDC) from photocathode materials. TESS illuminates the photocathode with a low-intensity beam (<10 pW) to ensure single-electron emission at femtoampere currents, tracking each electron's radial displacement on a phosphor screen. Electrons travel 35 mm in 8–25 ns, depending on the source–detector potential, producing footprints up to 8 mm radius. The transverse energy ε_{tr} is then extracted from the radial position using:

$$\varepsilon_{tr} = \frac{m_e}{2} \left(\frac{r}{\tau} \right)^2, \quad (2)$$

* saransh.malhotra@liverpool.ac.uk

where m_e is the electron mass, r is the measured footprint radius, and τ is the electron time of flight.

$$N_e(\varepsilon_{tr}) = \frac{dN}{d\varepsilon_{tr}} = \frac{2\pi\tau^2}{m_e} I_c(r). \quad (3)$$

In Eq. (3) $I_c(r)$ is footprint function and $N_e(\varepsilon_{tr})$ is TEDC as function of emittance. This work follows the methodology described in Ref. [2], where careful calibration and negligible space-charge effects allow TESS to achieve 1–2 meV resolution, enabling precise photocathode R&D and beam-brightness optimisation.

METHODOLOGY

Accurate MTE measurement is vital for optimising photocathodes. Our pipeline (Fig. 1) from data processing to physics-informed augmentation enables real-time MTE prediction and ML-based beam diagnostics.

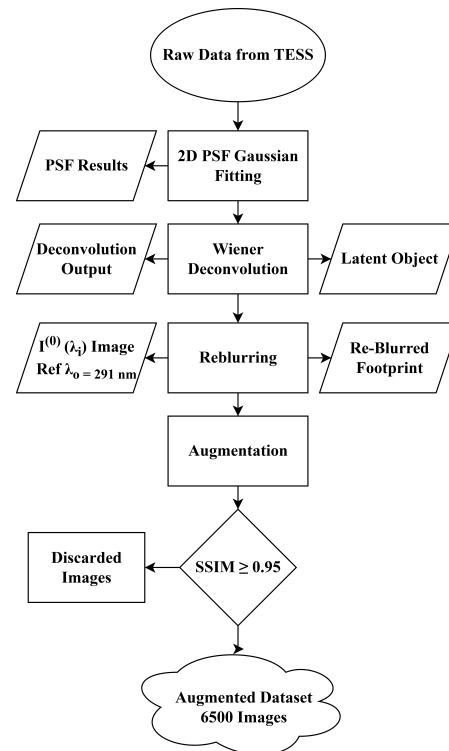


Figure 1: Flowchart summarising the complete TESS data processing and augmentation pipeline.

Single photoelectrons fall onto a microchannel plate (MCP) that generates a ‘beamlet’ which falls onto a phosphor

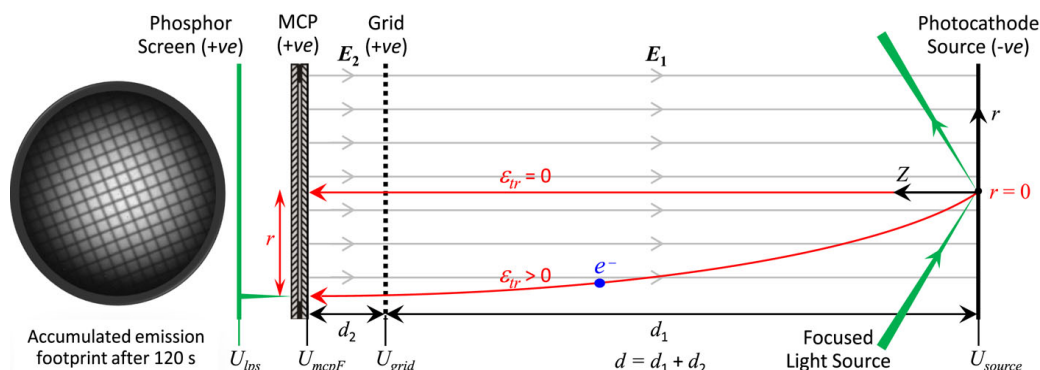


Figure 2: TESS concept showing a typical photoemission footprint acquired from $\approx 10^7$ electrons over 120 s integration [2].

screen. Data is then acquired using a CCD camera which images the integrated fluorescence generated by the phosphor screen over a period of approximately 100 s, thus yielding a photoemission footprint, see Fig. 2. Data were acquired for all photocathode illumination wavelengths from 231 to 291 nm in 5 nm steps. Each image undergoes preprocessing including dark-current subtraction, flat-field correction, and pixel intensity normalisation. Numpy was used to downscale the image to binary by still preserving the quality [4].

In the second step, quantitative characterisation is performed by fitting each image to a two-dimensional elliptical Gaussian function which defines photoemission footprint:

$$f(x, y) = Ae^{[-a(x-x_0)^2 - 2b(x-x_0)(y-y_0) - c(y-y_0)^2]} + \Omega^*. \quad (4)$$

Here, $f(x, y)$ is the pixel intensity at position (x, y) , A the peak amplitude, and (x_0, y_0) the centroid of the Gaussian. The cross-term coefficient b captures the x - y correlation. The expansion for each of the coefficients can be seen in the Appendix section. The additive term Ω^* models uniform background. This gives a full parametric description of a rotated elliptical PSF, capturing both intensity and shape. [5–7] (see Fig. 3).

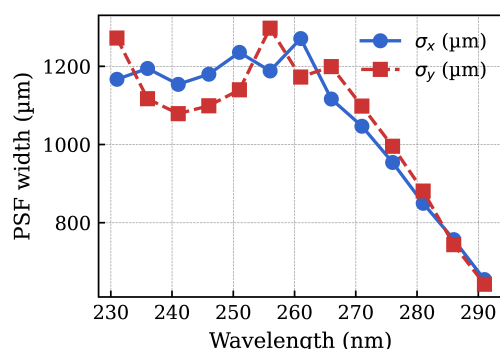


Figure 3: Measured σ_x and σ_y of the TESS PSF versus illumination wavelength, revealing wavelength-dependent changes in spatial resolution and emission anisotropy.

Next, the underlying (latent) electron emission distribution was recovered using Wiener deconvolution. In imaging

terms, each observed image $I(x, y)$ is a convolution of the latent emission pattern $f(x, y)$ with the PSF:

$$I(x, y) = \iint f(x', y') \cdot \text{PSF}(x - x', y - y') dx' dy'. \quad (5)$$

This convolution models spatial blurring from the imaging system. In the Fourier domain, Wiener deconvolution is given by Ref. [7]:

$$F(k_x, k_y) = \frac{H^*(k_x, k_y)}{|H(k_x, k_y)|^2 + \alpha} I(k_x, k_y), \quad (6)$$

where F is the Fourier transform of the latent image, H that of the PSF, H^* its complex conjugate, and α a regularisation constant (typically 10^{-4}). This value was explicitly chosen through empirical tuning and SNR optimisation to balance noise suppression and feature preservation. The inverse transform recovers $f(x, y)$ (See Fig. 4) [7]. For radially symmetric PSFs and profiles, the operation simplifies to a one-dimensional form via the zero-order Hankel transform the radial analogue of the 2D Fourier transform [8].

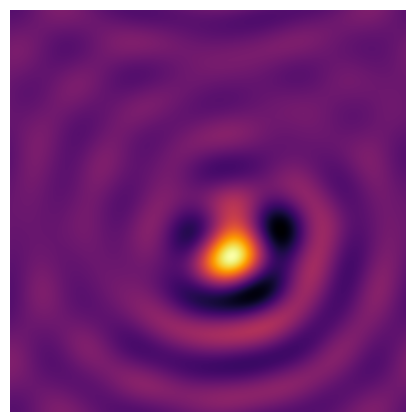


Figure 4: Wiener deconvolution restored the 236 nm TESS image, revealing a sharper latent emission profile with improved spatial resolution.

To ensure cross-wavelength consistency, all latent images were re-blurred to match the sharpest PSF (at 291 nm) [9]:

$$I_i^{(0)}(x, y) = f_i(x, y) * G(x, y; \sigma_{0x}, \sigma_{0y}), \quad (7)$$

$$G(x, y) = \frac{1}{2\pi\sigma_{0x}\sigma_{0y}} e^{-\left(\frac{x^2}{2\sigma_{0x}^2} + \frac{y^2}{2\sigma_{0y}^2}\right)}, \quad (8)$$

where G is a 2D Gaussian kernel with widths σ_{0x} , σ_{0y} . This convolution enforces uniform resolution across all wavelengths (see Fig. 5).

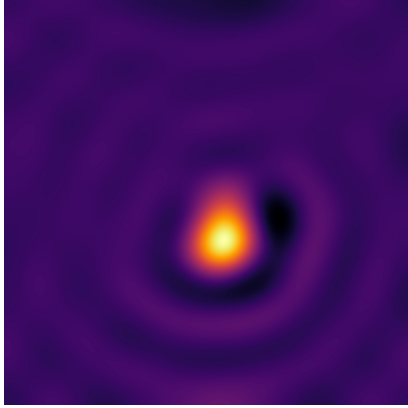


Figure 5: 236 nm latent emission re-blurred to match 291 nm resolution for consistent cross-wavelength comparison.

Finally, physics-informed augmentation was used to expand 13 re-blurred images into 6500 synthetic variants via rotations ($\pm 0.1 - 1^\circ$), sub-pixel shifts ($\pm 1 - 2 \mu\text{m}$), contrast jitter ($\pm 5\%$), and noise models (Poisson, Gaussian, CCD). Physically, these mimic beam pointing jitter, alignment errors, and detector noise, enabling robust beam-dynamics-aware ML models for emission characterisation. The need for a large number of variants is as it improves generalisation by covering wider input space and also it acts as a regularisation. Only images with an average structural similarity index measure (SSIM) ≥ 0.95 were retained [2, 10, 11] with representative results shown in Fig. 6.

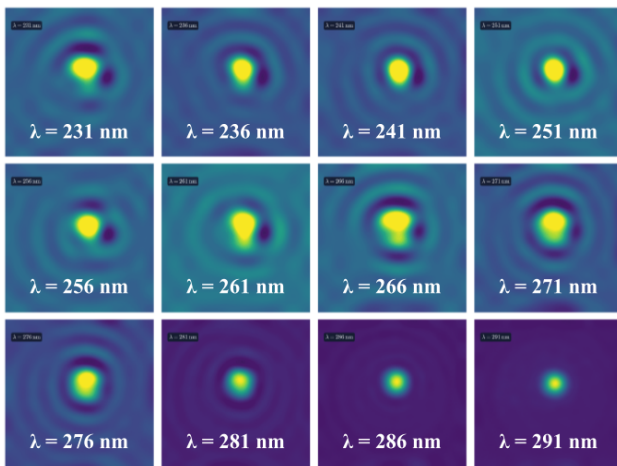


Figure 6: Representation of randomly picked augmented emission footprints following re-blurring and augmentation at different illumination wavelengths (12 of 13 shown).

RESULTS AND DISCUSSION

We developed a physics-informed image processing and augmentation pipeline for analysing photoemission profiles from the TESS system. Starting from 13 raw CCD images across ultraviolet wavelengths, we extracted two-dimensional Gaussian PSF parameters, applied Fourier-domain Wiener deconvolution to recover latent emission profiles, and standardised resolution by re-blurring to a common PSF at $\lambda_0 = 291 \text{ nm}$. The PSF widths, σ_x and σ_y , decreased with increasing wavelength, consistent with reduced MTE near the photoemission threshold. Using noise-aware augmentation, the pipeline expanded the dataset to 6500 physically consistent synthetic images, each labelled with wavelength, MCP gain, and estimated MTE derived from fitted Gaussian widths. The dataset demonstrated high fidelity (average SSIM = 0.99729, with all > 0.95) and strong correlation with ground truth ($R^2 \approx 0.98$). These results confirm that the method enables rapid, accurate photocathode characterisation and supports ML-based prediction and optimisation of emission properties for next-generation photoinjectors.

FUTURE DEVELOPMENT

Future work will integrate physics-informed deep learning models, including convolutional neural networks (CNNs), generative adversarial networks (GANs) and physics-informed neural networks (PINNs) to predict MTE and emission profiles directly from single-shot TESS images [12, 13]. The dataset may be extended to temporal sequences, enabling ultrafast photoemission tracking in video-TESS mode. Real-time MCP diagnostics and predictive control will aid beamline optimisation. Transfer learning across different materials could accelerate screening and discovery of photocathodes for next-generation electron sources and free-electron laser (FEL) injectors [14].

ACKNOWLEDGEMENTS

This work was supported by STFC through the LIV.INNO CDT (ST/W006766/1), the ASTeC core grant, and the Cockcroft Institute core grant (ST/V001612/1). Special thanks to Hugh Churn (STFC) for valuable guidance and assistance with data curation.

APPENDIX

$$a = \frac{\cos^2 \theta}{2\sigma_x^2} + \frac{\sin^2 \theta}{2\sigma_y^2}, \quad (9)$$

$$b = \frac{\sin(2\theta)}{4} \left(\frac{1}{\sigma_y^2} - \frac{1}{\sigma_x^2} \right), \quad (10)$$

$$c = \frac{\sin^2 \theta}{2\sigma_x^2} + \frac{\cos^2 \theta}{2\sigma_y^2}, \quad (11)$$

where θ is the rotation angle of the Gaussian ellipse.

REFERENCES

- [1] P. Saha *et al.*, “Theory of photoemission from cathodes with disordered surfaces”, *J. Appl. Phys.*, vol. 133, no. 5, Feb. 2023. doi:10.1063/5.0135629
- [2] L. B. Jones *et al.*, “The measurement of photocathode transverse energy distribution curves (TEDCs) using the transverse energy spread spectrometer (TESS) experimental system”, *Rev. Sci. Instrum.*, vol. 93, no. 11, Nov. 2022. doi:10.1063/5.0109053
- [3] M. A. H. Schmeißer, “Photocathodes for high brightness, high average current photoelectron injectors”, Ph.D. dissertation, Humboldt-Universität zu Berlin, Mathematisch-Naturwissenschaftliche Fakultät, 2019. doi:10.18452/20481
- [4] C. R. Harris *et al.*, “Array programming with NumPy”, *Ann. Sci. Nat. Zool. Biol. Anim.*, vol. 585, no. 7825, pp. 357–362, Sep. 2020. doi:10.1038/s41586-020-2649-2
- [5] C. Zhang, “A Method for Generating PSF Based on 2-D Fast Fourier Transform”, in *Proc. 2021 International Conference on Signal Processing and Machine Learning (CONF-SPML)*, Nov. 2021, pp. 229–233. doi:10.1109/conf-spml54095.2021.00051
- [6] H. Lei *et al.*, “Gaussian fitting algorithm with multi-geometric parameters for rotated elliptical beam profiling using pixel ion chamber”, *Biol. Med. Phys. Biomed. Eng.*, vol. 48, no. 9, pp. 4799–4811, Aug. 2021. doi:10.1002/mp.15140
- [7] R. C. Gonzalez, R. E. Woods, and B. R. Masters, “Digital Image Processing, Third Edition”, *J. Biomed. Opt.*, vol. 14, no. 2, p. 029901, 2009. doi:10.1117/1.3115362
- [8] S. Stallinga, N. Radmacher, A. Delon, and J. Enderlein, “Optimal transfer functions for bandwidth-limited imaging”, *Phys. Rev. Res.*, vol. 4, no. 2, Apr. 2022. doi:10.1103/physrevresearch.4.023003
- [9] F. Ji, J. Wang, S. Cui, J. Li, X. Tang, and F. Xu, “Physics-Guided Optical Simulation and PSF Analysis for Remote Sensing Images Deblurring”, *IEEE Trans. Geosci. Remote Sens.*, vol. 62, pp. 1–15, 2024. doi:10.1109/tgrs.2024.3426094
- [10] A. Foi, M. Trimeche, V. Katkovnik, and K. Egiazarian, “Practical Poissonian-Gaussian Noise Modeling and Fitting for Single-Image Raw-Data”, *IEEE Trans. Image Process.*, vol. 17, no. 10, pp. 1737–1754, Oct. 2008. doi:10.1109/tip.2008.2001399
- [11] J. T. Saminjonovich, T. D. Solijonovich, and I. M. F. Qizi, “Recognising visuals by artificial intelligence in the field of information security in religious educational organizations”, *ACADEMICIA: An International Multidisciplinary Research Journal*, vol. 13, no. 1, pp. 1–6, 2023. doi:10.5958/2249-7137.2023.00013.7
- [12] J. Slim *et al.*, “First detection of collective oscillations of a stored deuteron beam with an amplitude close to the quantum limit”, *Phys. Rev. Accel. Beams*, vol. 24, no. 12, Dec. 2021. doi:10.1103/physrevaccelbeams.24.124601
- [13] M. Raissi, P. Perdikaris, and G. E. Karniadakis, “Physics-informed neural networks: A deep learning framework for solving forward and inverse problems involving nonlinear partial differential equations”, *J. Comput. Phys.*, vol. 378, pp. 686–707, Feb. 2019. doi:10.1016/j.jcp.2018.10.045
- [14] E. A. Seddon and M. W. Poole, “The origins and development of free-electron lasers in the UK”, *Notes and Records: the Royal Society Journal of the History of Science*, vol. 78, no. 1, pp. 203–252, Feb. 2023. doi:10.1098/rsnr.2022.0038